

Chapter 2

Two-Body Interactions Between Li and Cs Atoms

In this chapter we investigate the binary scattering properties of an ultracold Li-Cs mixture and develop the theoretical and experimental framework, on which the further exploration of few-body effects that are discussed throughout this thesis will be based. We start by establishing the basic theoretical structure that is used to describe ultracold scattering in Sect. 2.2. We introduce the s -wave scattering length and show its intrinsic connection to the internal structure of the colliding atoms. This gives rise to magnetically tunable Feshbach resonances, and the weakly bound universal dimer, which is also known as the two-body quantum halo. We continue by presenting the typical experimental approach for producing an ultracold mixture of Li and Cs atomic gases in a single, predetermined scattering channel in Sect. 2.3. It is followed by the description of the two most crucial experimental techniques that are employed throughout this thesis for controlling and probing interactions, namely, homogenous magnetic field generation, and radio-frequency and microwave-frequency pulses. Finally, we explain the measurements of weakly bound LiCs Feshbach dimers and the procedure for obtaining the LiCs singlet and triplet molecular potential curves of the electronic ground state manifold with the help of coupled-channels calculation in Sect. 2.4. It yields, up to date, the most precise parametrization of Li-Cs scattering properties in the explored magnetic field range. This knowledge will be critical for appropriate analysis of three-body physics that is explored in Chaps. 3 and 4.

2.1 Interactions in Ultracold Mixtures of Li and Cs Atoms

The tunability of interactions between two ultracold, colliding particles is one of the most important capabilities of modern quantum gas experiments. The tuning is achieved by magnetic field dependent interparticle scattering resonances, called Feshbach resonances (FR), at which a two-body bound state crosses the scattering threshold. These resonances are routinely employed to tune the interaction strength between the colliding particles [1] and to produce weakly bound dimers by ramping up or down the external magnetic field [2]. They can be used to create strongly

correlated many-body systems [3], quasiparticles [4], and explore intriguing topics in few-body physics [5, 6]. However, the ability to study any of these fascinating systems, as well as the underlying principles, on which the behavior of such systems is based, relies on precise knowledge of the properties of the particular FR.

The central quantity that governs an ultracold collision process, and therefore most of the physics at such temperatures, is the two-body s -wave scattering length a . The inelastic three-body scattering rate near a FR scales as a^4 , resulting in magnetic field dependent atom losses that can be used to map out how a depends on the external field [9–11].

During the last decade such atom loss spectroscopy in combination with theoretical models has become a standard tool for the determination of specific interparticle interaction properties [1]. These methods yield an excellent representation of the overall FR spectrum. An example of such extensive atom-loss spectroscopy for Li-Cs Feshbach resonances [7, 12, 13] is shown in Fig. 2.1. In these measurements a total of 19 interspecies scattering resonances could be detected for the two energetically lowest spin states in the magnetic field range between 500 and 1000 G (only 7 of them are shown in the figure). The explanation of these atom-loss spectra relied on precise models of magnetic field-dependent scattering length. Excellent agreement was obtained by several numerical methods, including coupled-channels (cc) calcu-

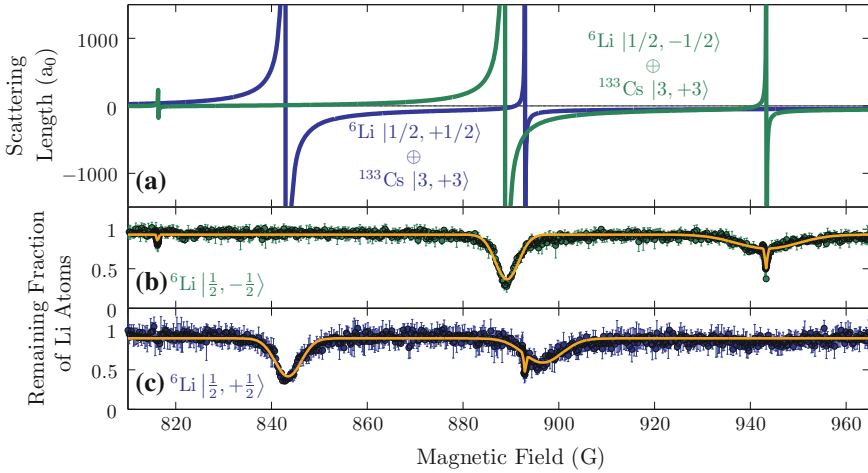


Fig. 2.1 Li-Cs s -wave Feshbach resonances for the two energetically lowest scattering channels [7]. **a** Scattering length dependence on the magnetic field for the two energetically lowest Li-Cs scattering channels. **b** and **c** trap loss spectra and Gaussian profile fits to the loss data for Li $|1/2, -1/2\rangle$ and Li $|1/2, 1/2\rangle$ spin states. Each feature in the loss spectra corresponds to a Feshbach resonance in the scattering length. The additional loss features correspond to Feshbach resonances due to different Cs spin states that are not shown here. Figure adapted from [8]

lation, asymptotic bound-state model (ABM), or multichannel quantum defect theory (MQDT) [8, 14]. All of the approaches describe the FRs with a sub-Gauss accuracy, thus the particular choice of the applied method depends on the required degree of precision for the final result and computational complexity. In this work we will exclusively use the cc approach, as it incorporates the least amount of assumptions out of the three models, and allows a straightforward calculation of the molecular energies required for FR pole determination (see Sect. 2.4).

Not all of the observed atom losses can be unambiguously attributed to an increasing two-body scattering length. Especially when a becomes large, not only immediate loss of three atoms from the trap, but also other processes, for example, weakly-bound dimer formation and subsequent secondary losses may occur. This can lead to shifts and asymmetric broadening of the loss signals [15–20] thus weakening the relation to the functional dependence of the scattering length alone. A precursor to such underlying dynamics can already be seen in the asymmetric loss profiles of the broad Li-Cs Feshbach resonances in Fig. 2.1.

More accurate mapping between the magnetic field and scattering length can be obtained by going further than a simple atom loss spectrum. The most precise scattering length measurements so far are delivered by direct radio-frequency (rf) [21–28] and magnetic field modulation [17, 29–36] spectroscopy of the least-bound molecular states. Since a FR intrinsically originates from the coupling of the scattering channel with such a molecular state, its energy E in the vicinity of the FR can be connected to the scattering length through the relation $E \propto a^{-2}$ [37, 38]. By mapping the magnetic field dependence of the binding energy of this state, it is possible to study exclusively the two-body problem, and the extraction of a is less prone to systematic effects. For the specific case of Li-Cs, we employ rf spectroscopy throughout this thesis, and in this way reduce the uncertainty of the Li-Cs Feshbach scattering length parametrization by almost a factor of 20 for the broad Feshbach resonances [39] in comparison to the initial atom-loss experiments [7, 13].

2.2 Low-Energy Scattering in Ultracold Quantum Gases

The elementary interaction mechanism of two neutral particles is a two-body collision in a potential that depends on the relative distance between them. In this section we shortly review the basic formalism of the scattering theory that is necessary to describe such process in the ultracold temperature regime where the dynamics are dominated by quantum threshold laws and single partial wave scattering. We start by recalling the concept of scattering length and collision cross section and their dependence on the quantum statistics in Sect. 2.2.1. It is followed by a discussion how the internal structure of the colliding particles leads to the emergence of Feshbach resonances that can be employed to control the interaction between the scattering partners in Sects. 2.2.2 and 2.2.3.

2.2.1 Basic Physics of Two-Body Scattering at Ultracold Temperatures

There exists many textbooks and lecture notes that treat the ultracold two-body scattering rigorously, see, for example, [40–45]. Here we give a short summary of the most important concepts that are required to understand the interaction between two colliding particles.

The Schrödinger equation in center-of-mass reference frame for two particles with mass m_1 and m_2 that interact through a potential $U(\mathbf{r})$ reads

$$\left[-\frac{\hbar^2}{2\mu} \nabla^2 + U(\mathbf{r}) \right] \psi(\mathbf{r}) = \frac{\hbar^2 k^2}{2\mu} \psi(\mathbf{r}), \quad (2.1)$$

where \mathbf{r} denotes the interparticle separation, $k = \sqrt{2\mu E}/\hbar$ is the wavevector of the relative motion for positive collisional energy E , and $\mu = m_1 m_2 / (m_1 + m_2)$ is the two body reduced mass. In general, the short-range part of the interaction potential $U(\mathbf{r})$ can take on any form. However we request that at large interparticle separation the potential vanishes, which corresponds to setting $U(\mathbf{r}) = 0$ for $|\mathbf{r}| \gg r_0$, where r_0 is a length scale that characterizes the short-range extent of the scattering potential. Then the wavefunction $\psi(\mathbf{r})$ in this region can be expressed by its asymptotic form

$$\psi(\mathbf{r}) = e^{ikr} + f(\theta, k) \frac{e^{ikr}}{r} \quad (2.2)$$

consisting of an incoming plane wave and an outgoing spherical wave with an angle θ and k dependent scattering amplitude $f(\theta, k)$.

With these basic constituents we can now introduce the partial wave expansion. Due to symmetry arguments for radial potentials $U(r)$ the scattering amplitude depends only on the angle θ between the colliding particle normal vectors, and the wavefunction can be expanded in the basis of spherical harmonics $Y_l^m(\theta, \phi)$ as

$$\psi(\mathbf{r}) = \sum_{l=0}^{\infty} \sum_{m=-l}^l Y_l^m(\theta, \phi) \frac{u_{k,l,m}(r)}{r}, \quad (2.3)$$

where $u_{k,l,m}(r)$ is the radial wavefunction that depends on k , the quantum number l that characterizes the angular momentum of the colliding particles and its projection m . Inserting this ansatz into the Schrödinger equation (2.1) one obtains

$$f(\theta, k) = \frac{1}{2ik} \sum_{l=0}^{\infty} (2l+1)(e^{2i\delta_l} - 1) P_l(\cos(\theta)), \quad (2.4)$$

where P_l denotes the Legendre polynomial, and we have introduced a phase shift δ_l between the incoming and outgoing wave. In the asymptotic region it quantifies the

effect of the short-range interaction potential on the scattering wavefunction and can be characterized by the Wigner threshold law $\delta_l \propto k^{2l+1}$ [46].

The quantum statistics of the particles plays a crucial role for the differential scattering cross section $d\sigma/d\Omega$ and total scattering cross section σ . The scattering wavefunction has to be properly symmetrized or antisymmetrized if the two colliding particles are identical bosons or identical fermions, respectively. This can be achieved by noting that $f(\theta, k) = -\varepsilon f(\pi - \theta, k)$ where $\varepsilon = +1$ for bosons and $\varepsilon = -1$ for fermions. By integrating the differential cross section $d\sigma/d\Omega = |f(\theta, k) + \varepsilon f(\pi - \theta, k)|^2$ over the solid angle Ω one can express the partial scattering cross section through

$$\sigma_l(k) = \frac{4\pi}{k^2} (2l+1) \sin^2 \delta_l, \quad (2.5)$$

from which the total cross section follows as $\sigma(k) = \sum_{l=0}^{\infty} \sigma_l$. Due to the imposed symmetry on the scattering wavefunction, $\sigma_l = 0$ if l is odd or even for identical bosons or identical fermions, respectively.

For scattering processes presented in this thesis, though, only scattering in the lowest partial wave $l = 0$, and consequently σ_0 , are relevant, since the experimentally employed temperatures are well below the centrifugal barriers originating from higher partial waves with $l > 0$ (see discussion in Sect. 2.2.2). Thus one introduces the s -wave scattering length a through the expression

$$a = \lim_{k \rightarrow 0} \frac{\tan [\delta_0(k)]}{k}, \quad (2.6)$$

as the only parameter characterizing an ultracold collision. Employing this definition one finally arrives at the following scattering cross section

$$\sigma(k) = \begin{cases} \frac{4\pi a^2}{1+k^2 a^2} & \text{for distinguishable particles,} \\ 0 & \text{for identical fermions,} \\ \frac{8\pi a^2}{1+k^2 a^2} & \text{for identical bosons.} \end{cases} \quad (2.7)$$

This result already demonstrates one of the most fundamental consequences of quantum statistics on ultracold scattering, namely, that identical fermions do not interact with each other through s -wave collisions. It will become important later in the analysis of the three-body recombination spectra in Sect. 3.4.

In ultracold gas experiments with neutral atoms the interaction potential $U(\mathbf{r})$ typically corresponds to the Born-Oppenheimer molecular potential, which is a spherically isotropic short-range potential. An interesting exclusion is the dipole-dipole interaction that gives rise to anisotropic potentials, and scattering that involves more partial waves than just the s -wave ($l = 0$). See, for example [47–51].

2.2.2 Scattering in External Magnetic Field

The ability to control the s -wave scattering length in ultracold neutral atomic and molecular gases that are subjected to external magnetic fields originates from the internal structure of the colliding particles. It gives rise to scattering resonances, called Fano-Feshbach resonances, in honor to Herman Feshbach and Ugo Fano who introduced the concept of energy dependent resonances due to coupling between a bound state and a continuum scattering state of two particles in nuclear physics [52] and atomic physics [53], respectively. The modification of this coupling by the externally applied magnetic field results in a change of the value of the scattering length and consequently interaction strength. A thorough review of Feshbach resonances in ultracold gases and the control of the scattering length is given in [1, 2]. Here we summarize the main results.

Consider the Schrödinger equation (2.1) and its Hamiltonian, which we now extend with an interaction term $H_{int} = H_{hf} + H_Z + H_{dd}$ to describe a binary collision in the presence of an external magnetic field [54]:

$$H = T + U + H_{int}. \quad (2.8)$$

In addition to the kinetic energy term $T = -\hbar^2 \nabla^2 / (2\mu)$ and potential U the Hamiltonian now contains the hyperfine energy operator

$$H_{hf} = \sum_{\xi=A,B} a_{hfs}^{(\xi)}(\mathbf{r}) \mathbf{s}_\xi \cdot \mathbf{i}_\xi \quad (2.9)$$

with the electronic and nuclear spin operators \mathbf{s}_ξ and \mathbf{i}_ξ , where the index ξ and the two terms in the sum correspond to the two atoms A and B . Here we consider the electronic ground state for alkali atoms $^2S_{1/2}$ with $l_\xi = 0$ and $s_\xi = 1/2$, as appropriate for the experiments presented in this thesis, and hence $\mathbf{j}_\xi = \mathbf{s}_\xi$. The separation dependent hyperfine constants $a_{hfs}^{(\xi)}(\mathbf{r})$ account for electronic distortions of one atom by the other at small separations [55], and asymptotically approach the atomic hyperfine constant A_{hfs}^ξ for $r \rightarrow \infty$. The Zeeman interaction is given by

$$H_Z = \frac{\mu_B}{\hbar} \sum_{\xi=A,B} (g_{s,\xi} \mathbf{s}_\xi + g_{i,\xi} \mathbf{i}_\xi + g_{l,\xi} \mathbf{l}_\xi) \cdot \mathbf{B}, \quad (2.10)$$

where the magnetic field \mathbf{B} couples to the electron spin, electron orbital, and nuclear magnetic dipole moments that are quantified with $g_{s,\xi}$, $g_{l,\xi}$, and $g_{i,\xi}$ gyromagnetic ratios, respectively. In general, the interaction Hamiltonian contains also magnetic dipole-dipole couplings between the different spin operators that are described by the term H_{dd} . These contributions, however, are small and present only in p-wave resonances, since an anisotropic interaction potential is required to generate experimentally observable energy shifts [56]. The work presented in this thesis deals exclusively with s -wave resonances, therefore, from here on, we neglect the H_{dd}

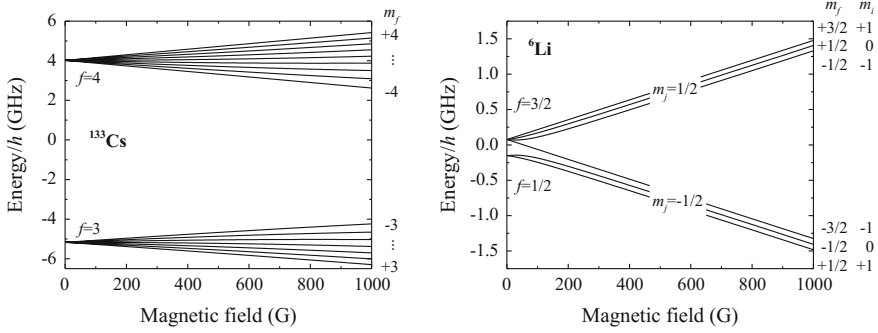


Fig. 2.2 Atomic energy levels of ^{133}Cs (left panel) and ^6Li (right panel) atoms as a function of the applied magnetic field in the electronic ground state. f denotes the total angular momentum of the atom and m_f , m_j , and m_i are the magnetic total, electron spin, and nuclear spin quantum numbers, respectively

term in the interaction Hamiltonian. Its effective form and explicit application for the Li-Cs system can be found elsewhere [8].

Figure 2.2 shows the calculated atomic hyperfine energy levels as a function of the applied magnetic field for ground state ^{133}Cs and ^6Li atoms that corresponds to the eigenenergies of H_{int} (see Eq. (2.8)). The hyperfine energy levels are labeled by their total angular momentum $f = |\mathbf{j} + \mathbf{i}|$ and its projection m_f on the quantization axis. For high magnetic field strengths the Zeeman energy becomes large in comparison to the hyperfine splitting, and consequently f is not a good quantum number anymore, while m_f is still a good one due to rotational symmetry around the magnetic field axis that we choose as the quantization axis. The individual quantum numbers allows one to define a scattering channel with the quantum number $M_F = m_{f,A} + m_{f,B}$ that is characterized by the state $|\zeta\rangle = A |f_A, m_{f,A}\rangle \oplus B |f_B, m_{f,B}\rangle$, also called scattering channel, and asymptotically corresponds to two noninteracting atoms in free space described by the combination $f_{\xi}, m_{f,\xi}$ for each atom. The scattering channels can be separated into two groups. A channel is called open (closed) if the initial energy E of the colliding atoms is larger (smaller) than its asymptotic energy, which corresponds to the sum of the internal energies of two atoms in the limit $r \rightarrow \infty$.

In this work we experimentally employ the energetically lowest Cs spin state with $f = +3$ and $m_f = +3$, and the two energetically lowest Li spin states with $f = +1/2$ and $m_f = +1/2; -1/2$ (see Fig. 2.2). For these energy levels we define the appropriate scattering channels by

$$\begin{aligned} |\alpha\rangle &= \text{Li} \left| \frac{1}{2}, +\frac{1}{2} \right\rangle \oplus \text{Cs} |3, +3\rangle, \\ |\beta\rangle &= \text{Li} \left| \frac{1}{2}, -\frac{1}{2} \right\rangle \oplus \text{Cs} |3, +3\rangle. \end{aligned} \quad (2.11)$$

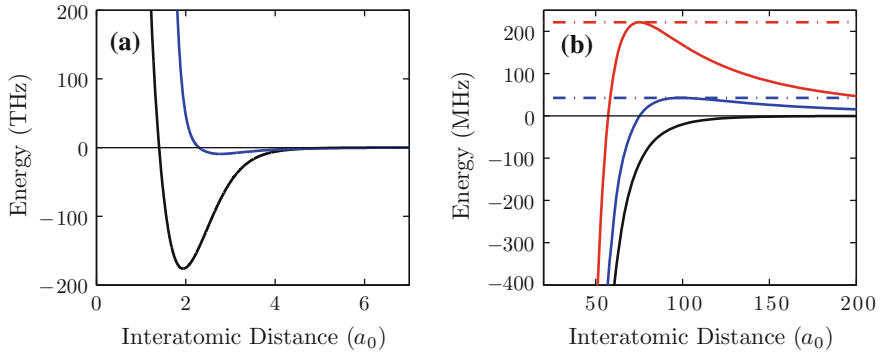


Fig. 2.3 Born-Oppenheimer molecular potentials of the LiCs electronic ground state. **a** Full singlet (black) and triplet (blue) potentials as calculated from a coupled channels calculation. **b** Long range van der Waals potentials with $l = 0$ (black), $l = 1$ (blue), and $l = 2$ (red) centrifugal terms. The dash-dotted lines illustrate the rotational barrier; see Eq. (2.12). Figure adapted from [8]

The projections M_F for channels $|\alpha\rangle$ and $|\beta\rangle$ yields values $M_F^{(\alpha)} = 7/2$ and $M_F^{(\beta)} = 5/2$, respectively. The kinetic energy in the experiments presented here is on the order of ~ 10 kHz¹ and the typical energy separation between consecutive scattering channels is on the order of tens of MHz. Thus, if the system is prepared in $|\alpha\rangle$ or $|\beta\rangle$ channel, there is one or two open channels, respectively.

The scattering channels with different M_F are diagonal in the interaction Hamiltonian H_{int} representation. Once additional terms are introduced in the Hamiltonian, the scattering channels can be coupled. The interatomic potential $U(\mathbf{r})$ is an important example, since exactly this coupling is responsible for the existence of Feshbach resonances (see Sect. 2.2.3). However, the scattering channels can be coupled also through other mechanisms, for which oscillating magnetic fields is an prime example. This will become important for the discussion of the radio-frequency association of Feshbach dimers in Sect. 2.4.

Now we turn our attention to the interatomic potential $U(\mathbf{r})$, specifically, we consider spherically isotropic potentials, which allows one to drop the vector notion. For interactions between two alkali atoms it corresponds to the Born-Oppenheimer molecular potentials, which are shown in the Fig. 2.3a for the LiCs dimer ground electronic state. The two potential curves differ by the orientation of the valence electron spins, as they can arrange themselves in either singlet ($S = 0$) or triplet ($S = 1$) configuration, where the total electron spin $S = s_A + s_B$. This leads to a significant difference between the molecular binding energies for the two arrangements, and the total potential $U(r) = P_0 U_0 + P_1 U_1$ has to be constructed as a superposition of the singlet and triplet contributions by projection operators P_0 and P_1 , respectively.

By transforming the Schrödinger equation (2.1) into the spherical coordinate system an effective rotational potential barrier emerges, which adds to the radial

¹If expressed in the appropriate units $1 \mu\text{K}$ is equivalent to 20.8 kHz.

potential energy seen by the atoms (see Fig. 2.3b). Its amplitude U_{rot} can be expressed as

$$U_{rot} = \frac{1}{\sqrt{2C_6}} \left(\frac{\hbar^2 l(l+1)}{3\mu} \right)^{3/2} \quad (2.12)$$

that depends on the particular partial wave l , in which the two particles are colliding. The amplitude of the potential barrier is on the order of 2 and 11 mK for Li-Cs p -wave ($l = 1$) and d -wave ($l = 2$) collisions, respectively. The experimentally employed temperatures range from 1 μ K down to a couple of tens of nK, thus effectively screening the particles colliding in higher partial waves from exploring the short internuclear distances where the interspecies potential $U(r)$ is significant. This estimation confirms that the use of the s -wave scattering length a , as introduced in Sect. 2.2.1, is well suited for the description of the entire scattering process.

2.2.3 Interactions and Weakly-Bound Dimers Close to a Feshbach Resonance

A Feshbach resonance emerges if the energy of an atom pair that is scattering in the entrance scattering channel matches the one of a bound state that is supported by a closed channel, and a coupling exists between them. If the magnetic moments of the involved channels are different, the energy difference can be controlled via an external magnetic field. This gives rise to magnetic field dependent coupling and, consequently, scattering length. Scattering theory provides an elegant way of calculating the transition amplitudes between the involved channels. In order to illustrate the basic concepts we shortly recapture the two-channel scenario that was first introduced in [57] and further elaborated in [2, 38, 58, 59].

The starting point is the Schrödinger equation and Hamiltonian from Eq. (2.8), which we project onto the open and closed channel subspaces via the projection operators \hat{P} and \hat{Q} , respectively. One obtains a set of coupled equations

$$(E - H_{PP})\Psi_P = H_{PQ}\Psi_Q \quad (2.13)$$

$$(E - H_{QQ})\Psi_Q = H_{QP}\Psi_P, \quad (2.14)$$

where the projection onto the respective open and closed subspaces is denoted by subscripts P and Q. Here $H_{i\hat{j}} = \hat{i}H\hat{j}$, and $\Psi_i = \hat{i}\Psi$ and the total scattering wavefunction

$$\Psi = \sum_{\zeta} \psi_{\zeta}(\mathbf{r}) |\zeta\rangle, \quad (2.15)$$

which is expanded over the basis of the scattering channels $|\zeta\rangle$ and r dependent coefficients $\psi_{\zeta}(\mathbf{r})$. Equation (2.14) can be formally solved by Green's operator $1/(E - H_{QQ} + i0)$, which yields

$$\Psi_Q = \frac{1}{E - H_{QQ} + i0} H_{QP} \Psi_P. \quad (2.16)$$

Substitution of this solution back into Eq. (2.13) gives an effective expression for the scattering process in the open channel that reads

$$\left(H_{PP} + H_{PQ} \frac{1}{E - H_{QQ} + i0} H_{QP} \right) \Psi_P = E \Psi_P. \quad (2.17)$$

This Schrödinger equation illustrates the basic mechanism behind a Feshbach resonance. The second term in the effective Hamiltonian can be interpreted as a transition from open P-subspace to closed Q-subspace, followed by propagation in Q-subspace, and completed by re-emission back into P-subspace. The phase shift acquired by the wavefunction during this propagation is reflected in the modification of the scattering length a , which was introduced in Eq. (2.6). The first term H_{PP} is present also if no closed channels exist, and hence it corresponds to a pure scattering process in the open channel subspace P, where its primary role is to give rise to the background scattering length a_{bg} . The couplings H_{PQ} and H_{QP} are determined by the Coulomb interaction, to which the main contribution arises from electron exchange that is proportional to the energy difference between the singlet and triplet molecular potentials.

The object that characterizes the collision process in a multichannel system is the unitary scattering matrix S . Matrix elements S_{ji} quantify the transition amplitudes from an incoming channel i into an outgoing channel j . For a single channel the S -matrix element is related to the scattering phase shift $\delta(k)$ via relation $S(k) = e^{2i\delta(k)}$, and the elastic cross section can be expressed as $\sigma_\zeta = g_\zeta \pi / k^2 |1 - S_{\zeta\zeta}|^2$, where g_ζ characterizes the quantum statistics of the colliding particles [1].

Let us investigate the behavior of the matrix element S_{ii} in case when the total energy E is close to a discrete bound state energy ε_B and there is only one open channel. This is known as the single resonance, two-channel approach [2, 57–59] and requires an energy spacing between the discrete energy levels of H_{QQ} that is much larger than any of the near-threshold couplings, kinetic and potential energy distributions. One can easily show that this is the case for typical experiments with ultracold gases. Particularly, for an ultracold mixture prepared in the energetically lowest spin states the single energetically allowed outgoing channel is also the incoming channel. Thus, the S matrix reduces to a single element, which can be written as [57]

$$S = S_{bg} \left(1 - \frac{i\Gamma(E)}{E - \varepsilon_B - \mathcal{A}(E)} \right), \quad (2.18)$$

where $\Gamma = 2\pi |\langle \psi_B | H_{PQ} | \zeta^+ \rangle|^2$ describes the coupling between the corresponding molecular eigenstate $|\psi_B\rangle$ and the incoming part of the scattering state, which is denoted by $|\zeta^+\rangle$, and ε_B denotes the energy of the molecular state (bare energy) in the closed subspace Q. S_{bg} describes the scattering in the open P-channel, and $\mathcal{A}(E)$ is the complex energy shift that is expressed by

$$\mathcal{A}(E) = \langle \psi_B | H_{QP} \frac{1}{E - H_{PP} + i0} H_{PQ} | \psi_B \rangle, \quad (2.19)$$

decomposed as $\mathcal{A}(E) = \Delta(E) + i\Gamma(E)/2$ into a real part $\Delta(E)$ and an imaginary part $\Gamma(E)$. For energies above the scattering threshold ($E > 0$), the molecular state with the bare energy ε_B can be interpreted as a quasi-bound state in the Q-subspace that is shifted by $\Delta(E)$ due to the couplings to the P-subspace, and has a width $\Gamma(E)$. For negative energies ($E < 0$) the energy shift $\mathcal{A}(E)$ is real, and hence it describes an actual energy shift of the bare molecular state due to coupling to the scattering channel.

In our experiments, the closed and open scattering channels consist of a pair of atoms in different hyperfine states, so the two channels exhibit different magnetic moments. This leads to magnetic field dependent differential energy shifts between ε_B , E , and $\mathcal{A}(E)$. Thus, if a bound state in the closed channel is close enough to the scattering threshold, one can bring them into degeneracy by changing the external magnetic field. Therefore, we consider ultracold scattering where only the s -waves contribute, and the relative collision energy $\varepsilon_r = E - E_{th} \sim k^2$, where E_{th} is the threshold energy. Noting that $S = e^{-2ika}$ and $S^{bg} = e^{-2ika_{bg}}$, the magnetic field dependence of the scattering length can be expressed as

$$a(B) = a_{bg} - \frac{\pi \hbar m}{\epsilon_{res}} \Gamma(B), \quad (2.20)$$

where $\epsilon_{res} = \varepsilon_B(B) + \Delta(B)$ in the zero-energy limit. By introducing the explicit B-dependence of $\epsilon_{res}(B) = (\mu_P - \mu_Q)(B - B_{FR})$ on the magnetic moments μ_P and μ_Q of an asymptotically separated pair of atoms in the scattering channel and the molecular state, respectively, this equation recovers the well-known dispersive expression for Feshbach resonances

$$a(B) = a_{bg} \left(1 - \frac{\Delta B}{B - B_{FR}} \right), \quad (2.21)$$

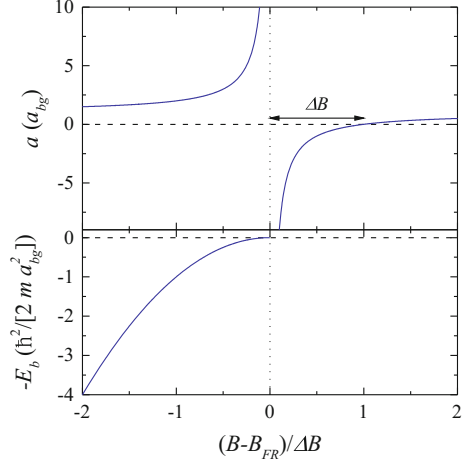
which is parametrized by the resonance pole position B_{FR} and width ΔB , quantifying the coupling strength between the P and Q subspaces. This behavior is shown in Fig. 2.4 for a generic Feshbach resonance. In general, a_{bg} and ΔB contains a weak dependence on B , however for near-resonant scattering close to the pole of a Feshbach resonance this dependency is negligible in comparison to the resonant behavior.

According to Eq. (2.18), the energy of the molecular state in the vicinity of the pole of the Feshbach is given by

$$E_b = \varepsilon_B + \mathcal{A}(E_b), \quad (2.22)$$

which consists of the bare energy ε_B of the closed subspace Q that is “dressed” by the coupling to the scattering channel in the open subspace P . For energies below the scattering threshold the expression reduces to $E_b = \varepsilon_B + \Delta(E_b)$. In the limit

Fig. 2.4 Structure of a generic Feshbach resonance. The *upper panel* shows the scattering length given by Eq. (2.21) with the zero-crossing located one resonance width ΔB away from the pole position B_{FR} . The *lower panel* depicts the universal energy dependence of the “dressed” molecular state (quantum halo state), given by Eq. (2.23)



$E_b \rightarrow 0$ and $B \rightarrow B_{FR}$, the real part of the complex energy shift vanishes, i.e. $\Delta(0) \rightarrow 0$, which implies that the properties of the near-resonant molecular state are solely determined by the properties of the scattering state, and consequently a . Therefore, this regime and the molecular state are usually referred to as the universal regime and quantum halo or universal dimer state. A rigorous derivation of this relation is given in [2, 38], and relies upon an explicit determination of the energy dependence of the complex energy shift $\mathcal{A}(E_b)$. Here, we give only the final result [2]

$$E_b(B) = \frac{1}{2m} \left(\frac{\hbar}{a_{bg}} \frac{B - B_{FR}}{\Delta B} \right)^2, \quad (2.23)$$

which is also shown in Fig. 2.4. In the limit of large scattering lengths $a \gg a_{bg}$ and in combination with Eq. (2.21) it reduces to the well-known universal formula for the bound-state energy of a weakly bound dimer:

$$E_b = -\frac{\hbar^2}{2ma^2}. \quad (2.24)$$

2.3 Producing and Probing Ultracold Li-Cs Mixtures

In this section we discuss our approach for the preparation of an ultracold Li-Cs mixture, which is used to obtain ensembles of ultracold Li and Cs atoms in a single scattering channel with temperatures ranging from around 500 nK down to approximately 250 nK. Even lower temperatures can be reached in this experimental setting for single species, evidenced by the observation of Bose-Einstein condensation of Cs atoms and Li₂ molecules during this thesis. Details on the relevant experimental

procedures can be found in [8, 12, 60]. In this chapter we exemplify our experimental sequences by discussing the mixture preparation at around 400 nK, which is largely unaffected by the gravitational sag. The design of experimental apparatus, cooling and imaging techniques have been already presented in great detail in [8, 12, 60–63]. Therefore, we start by introducing the experimental cooling sequence that was employed in the experiments with weakly bound LiCs molecules and, in part, the observation of Li-Cs-Cs Efimov resonances. Since magnetic and radio-frequency fields play a crucial role not only in the two-body sector, but also for three-body physics, we shortly describe their most important characteristics, especially the determination of the systematic errors for homogenous offset and oscillating (with radio- and micro-wave frequency) magnetic fields.

2.3.1 Experimental Procedure for the Sample Preparation at 400 nK

The overview of our experimental preparation sequence is given in Fig. 2.5. We start by loading a Cs MOT for typically 2 s, followed by two degenerate Raman sideband cooling [64–66] cycles of approximately 15 ms that spin polarize the atoms to about 90% in the energetically lowest Zeeman state $\text{Cs}|f = 3, m_f = +3\rangle$. The second cycle is performed already with the reservoir trap turned on at 35 W. As the atoms in the wings of the trap are heated due to the conversion of higher potential into kinetic energy, it is beneficial to apply the second pulse after a short propagation period in the optical dipole potential, during which more of the atoms have reached the center of

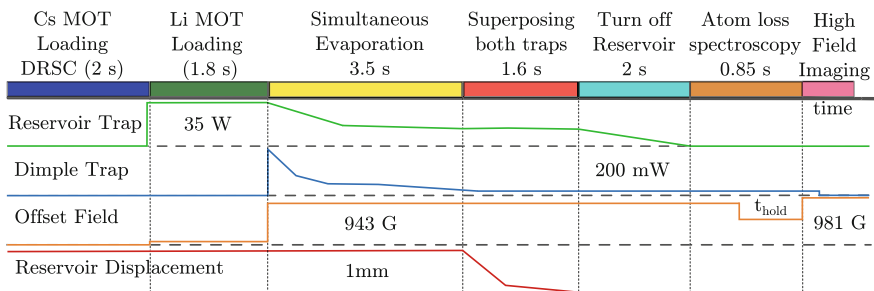


Fig. 2.5 Experimental sequence for the preparation of Li-Cs mixture near the 843 G Feshbach resonance in the scattering channel $|\alpha\rangle$. This sequence represents the general cooling and mixing approach of the two atomic species that is used for the characterization of the experimental setup and for the observation of the Efimov resonances at 450 nK temperatures. The experiments on radio-frequency association of LiCs dimers follow the same approach with slightly different magnetic field values for the offset field, which are given in the text. Figure adapted from [8]

the trap.² In this way an approximate two-fold increase in final phase-space density in the reservoir trap is achieved. At this point we apply an offset magnetic field of ~ 4.5 G to preserve the spin polarization by providing a quantization axis.

The sequence is continued by a spatially separated loading of a Li MOT for 1.8–2.5 s. After a short compression phase the Li atoms are loaded into the dimple trap at ~ 1 mm displacement from the reservoir trap, in which Cs atoms are being held. At the end of the MOT phase we apply a short optical pumping pulse that transfers all of the Li atoms into the $f = 1/2$ hyperfine state. Since we have not applied any spin polarization techniques so far, Li atoms populate both of the Zeeman sublevels, namely, $\text{Li}|f = 1/2, m_f = +1/2\rangle$ and $\text{Li}|f = 1/2, m_f = -1/2\rangle$.

At this point we set the homogenous offset field to $B_{\text{evap}} \approx 920$ G to ensure rapid thermalization of both species, and perform simultaneous forced evaporation with still spatially separated reservoir and dimple traps. After approximately 3.5 s long evaporation ramp, we superimpose both traps with a piezo-driven mirror within one fast (600 ms) and one slow ramp (1 s) to ensure approximately adiabatic merging. While keeping the power in the dimple trap constant, we turn off the reservoir trap in a 2 s long ramp, which transfers a part of the Cs atoms into the dimple trap. As the potential depth decreases the temperature of the gas in the reservoir trap is further reduced. Because these atoms are still in thermal contact with the ones in the dimple trap due to collisions, the thermal energy can be exchanged, which leads to cooling in the dimple trap as well, and equal temperature in both of the traps. Additionally, the local increase in the trapping frequencies leads to increased phase space density in the dimple trap, which is often in the literature referred to as the *dimple trick* [67–69].

During the last ramp of the reservoir trap the atom clouds already overlap. The ramp is performed at $B_{\text{mix}} \approx 875$ G to minimize three-body losses of Cs atoms while still ensuring high enough scattering cross section for intra and interspecies collisions. This value was experimentally found to optimize the remaining number of atoms in all the three different spin states of both species after the reservoir trap had been ramped off.

The mixed sample in the dimple trap now consists of Cs atoms in spin state $|3, +3\rangle$ and Li atoms in spin states $|1/2, +1, 2\rangle$ and $|1/2, -1/2\rangle$. The final scattering channel $|\alpha\rangle$ or $|\beta\rangle$ (see Eq. (2.11) for the definition of the scattering channels) is selected by shining in a laser light pulse that is resonant with the D2 transition of $\text{Li}|1/2, -1/2\rangle$ or $\text{Li}|1/2, +1/2\rangle$ spin states at the given magnetic field, thus removing the unnecessary spin component. After a slight re-compression of the dimple trap in 500 ms, that stops the residual evaporation, but increases the final temperature to about 450 nK, we are left with about 4×10^4 Li and 4×10^4 Cs atoms in the necessary scattering channel. At these conditions we measure the secular trapping frequencies f_x, f_y, f_z of 11, 114, 123 Hz (33, 275, 308 Hz) for Cs (Li) atoms, where the external magnetic field is parallel to the z axis. This procedure is discussed in detail in [8, 12, 61].

²Note that in a harmonic trap the oscillation period is the same, independent at which potential energy the oscillation is started.

2.3.2 Homogenous Magnetic Fields

The magnetic fields are of fundamental importance for all of the measurements performed in this thesis. As explained in Sect. 2.2, the use of magnetic Feshbach resonances allows one to change the magnitude and sign of the scattering length, which is an essential ingredient for the observation of Efimov physics. Furthermore, the energy of the weakly bound molecular state that gives rise to the scattering resonance also tunes with the applied magnetic field (see Sect. 2.2.3). In fact, exactly this connection allows one to infer the structure of the scattering resonance and its relation to the magnetic field, as presented in Sect. 2.4.

Here we explain the main characteristics of our setup for generating homogenous magnetic fields, which are used to control and tune the properties of ultracold atomic samples in all of the measurements that are presented in this work. In the next paragraphs we highlight two of the most relevant magnetic field properties for the performed experiments: the long-term stability and the switching speed. We do not discuss the technical setup, since it has already been described in detail elsewhere [8, 12].

The stability of magnetic fields that is on the order of a couple of mG is crucial. To illustrate this let us consider the behavior of scattering length in the vicinity of a Feshbach resonance, given by Eq. (2.21). As the uncertainty in the magnetic field increases, the ability to resolve scattering length close to the pole of the resonance diminishes. The maximum value that can be still resolved can be estimated employing Gaussian error propagation. The uncertainty of scattering length δa , which is caused by magnetic field uncertainty δB , is given by

$$\delta a = \frac{a_{bg} \Delta B}{(B - B_{FR})^2} \delta B. \quad (2.25)$$

By loosely defining the theoretical resolution limit at the magnetic field value, for which $\delta a(B) = a(B)$, Eq. (2.25) yields $\delta a_r \approx a_{bg} \Delta B / \delta B$, for $(B - B_{FR}) \ll \Delta B$. We can apply this estimation for the case of Li-Cs Feshbach resonances by choosing a hypothetical resonance that approximately mimics Li-Cs ones. Using width $\Delta B = 60 \text{ G}$ and $a_{bg} = 30 a_0$ we obtain $\delta a_r \approx 10^5 a_0$ for magnetic field uncertainty $\delta B = 16 \text{ mG}$, which is the value that is achieved with the experimental setup. Although δa_r quantifies the largest scattering length that can be distinguished from the pole, in practical applications the resolution will be lower, since, instead of the pole, one is interested in resolving resonant features close to it, for which more than one point is necessary.

The magnetic field uncertainty for the performed experiments originates from the following sources:

- Calibration of magnetic fields. The calibration of magnetic fields is typically performed over 5 to 6 uniformly distributed values within the magnetic field range at which the measurements are taken. The resulting dependence of the magnetic field values on the control parameter is fitted with a linear function, which is later used

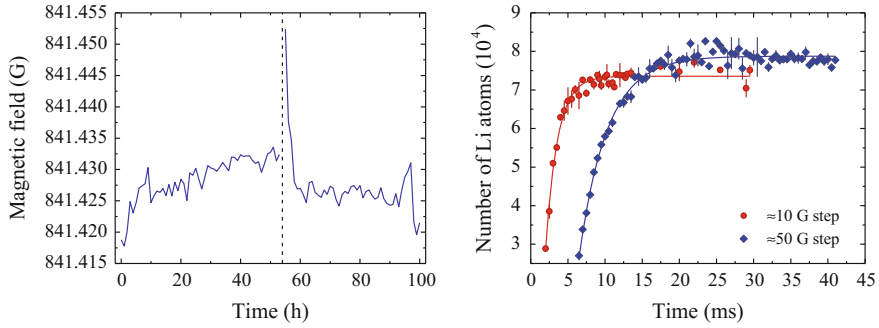


Fig. 2.6 Long-term stability (*left panel*) and step response (*right panel*) of magnetic fields. In the left panel, each data point is obtained from an independent determination of magnetic field by rf-spectroscopy of Li (see Sect. 2.3.3). The *vertical dashed line* shows the time when the execution of the experimental sequence was paused and resumed after several hours. The *solid lines* depict fits of an exponential growth equation to the data, with time constants 1.6 and 3.8 ms for 10 G (*red circles and line*) and 50 G (*blue diamonds and line*) step size, respectively

to infer the magnetic field value for the given control parameter. This procedure introduces an magnetic field uncertainty of 9 mG. For calibration we use radio-frequency spectroscopy to drive transitions between Li hyperfine states, which is described in detail in Sect. 2.3.3.

- Long-term stability. The magnetic field calibration is performed once every several days, during which the absolute value of the field with respect to the control parameter may vary. To characterize this variation an extended series of measurements was taken, which is depicted in the left panel of Fig. 2.6. After the experimental setup has thermalized and reached a steady state, which may take a little bit longer than a day, if initialized from completely “cold” state (not shown in the figure), the fluctuations of the absolute value of magnetic field stay within ≈ 10 mG. In fact, the maximum standard deviation from the mean during the course of a 24 h period is 8 mG, which we use as the uncertainty quantifying the long-term drifts. To estimate the time that is necessary for the experimental system to reach the steady state after a short break, we stopped the execution of the experimental sequence (vertical dashed line in Fig. 2.6 (left panel)) and resumed the operation after several hours. Within three to four hours of continuous operation the magnetic field stabilizes to the previous level.
- Experimental sequence length. The steady state conditions may depend on the length of the experimental sequence. For example, due to the generated ohmic heat that is deposited in the magnetic field coils their geometry may change, which would lead to a different absolute value of the applied field. We quantify this uncertainty by comparing magnetic field calibration immediately after the sample preparation (see Sect. 2.3.1) and after 3000 ms. The difference is 8 mG, which is included in the total uncertainty.
- Residual magnetic field gradient. Since the magnetic coil setup deviates from an exact Helmholtz configuration, the final field in which the atoms are located may

exhibit rest-gradient [8, 12]. The upper limit of this uncertainty is estimated from the linewidth of the Li electron spin flip transition as described in Sect. 2.3.3, yielding 8 mG.

We assume that these sources are uncorrelated and use simple addition of squares to extract the total systematic uncertainty, which results in 16 mG.

An important component of any experimental sequence is the switching of magnetic fields, especially the time that is necessary for the field to stabilize to the new value after the control parameter has been changed. Since the performed experiments rely on extracting different observables as a function of magnetic field, the short term stability of the field is critical, therefore we optimize the experimental sequence in such a way that the measurements are taken only after the field has stabilized.

In order to determine the necessary wait time, we recorded the step response of our magnetic coil setup, which is depicted in the right panel of Fig. 2.6. Here, a sample of Li atoms in $|1/2, +1/2\rangle$ spin state was prepared and the magnetic field was suddenly switched to 870 G. Immediately after setting the new value a $190\text{ }\mu\text{s}$ long π -pulse was applied that, in case of no additional Zeeman shifts, would transfer all of Li atoms into $|1/2, -1/2\rangle$ spin state, which was being imaged. Depending on the amplitude of the magnetic field step size, an fit of the exponential growth model $N(t) = N_0 + C(1 - e^{-t/\tau})$ to the data yields time constant $\tau = 1.6\text{ ms}$ or 3.8 ms for 10 G or 50 G step size, respectively. Here, $N(t)$ denotes the time-dependent number of atoms, N_0 stands for the initial number of atoms and C is an amplitude constant. Typically we start recording data after a wait time of approximately five to ten time constants.

2.3.3 Radio- and Microwave Frequency Fields

In the context of this thesis, microwave (mw) and radio-frequency (rf) spectroscopy is used to measure the energy difference between two energy eigenstates of a system consisting of atoms or molecules that are confined in an external potential. The system is exposed to a mw or rf pulse that induces population transfer from one eigenstate into another. Since the experimentally employed samples are very dilute, this process is well described by a two-level system, which allows one to drive Rabi oscillations between the eigenstates or perform rapid adiabatic passages in order to prepare the required scattering channel. Additionally, from the energy of the applied photon one can infer the energy difference between the two eigenstates of the system. Since typical linewidths of these transitions are very narrow, these techniques are well suited for precision measurements of such energy differences in ultracold gas experiments.

In our measurements three different transitions are employed (for Breit-Rabi energy level diagrams and corresponding quantum numbers see Fig. 2.2):

- (i) Nuclear spin flip transition between $\text{Li}|1/2, +1/2\rangle$ and $\text{Li}|1/2, -1/2\rangle$ Zeeman sublevels with $\Delta m_i = 1$ (also referred to as free-free transition in the context of LiCs dimer association, see Sect. 2.4),
- (ii) Electron spin flip transitions from $\text{Li}|1/2, +1/2\rangle$ to $\text{Li}|3/2, 3/2\rangle$, and from $\text{Li}|1/2, -1/2\rangle$ to $\text{Li}|3/2, 1/2\rangle$ Zeeman sublevels with $\Delta m_j = 1$,
- (iii) Nuclear spin flip transitions starting in the Li-Cs scattering channels $|\alpha\rangle$ and $|\beta\rangle$ (see Eq. (2.11)), and the corresponding molecular state $|\psi_B^\beta\rangle$ and $|\psi_B^\alpha\rangle$, respectively, with $\Delta m_i = 1$.

Here, Δm_i and Δm_j indicates selection rules of magnetic quantum numbers for nuclear and electron spin flip transitions, respectively. For type (i) and (iii) transitions the difference between the energy eigenstates is $\sim h \times 76$ MHz in the magnetic field range from 800 G to 900 G, hence they are referred to as rf-transitions. Type (ii) transitions are referred to as mw-transitions because they require driving fields at frequencies that are around 2 GHz.

In what follows, we shortly discuss our application of type (i) and (ii) transitions for the characterization of the magnetic field setup and entrance scattering channel preparation. Type (iii) transitions in this work are used for weakly bound LiCs dimer production and their rf-spectroscopy, and are described in more detail in Sect. 2.4.

A spectrum of a type (i) transition at 888.535 G magnetic field is shown in the left panel of Fig. 2.7. We employ the resonance frequency of the transition in conjunction with the Breit-Rabi formula to calibrate the absolute magnetic field strength, as described in Sect. 2.3.2. In order to do this, we fit the data points with the lineshape function, given by

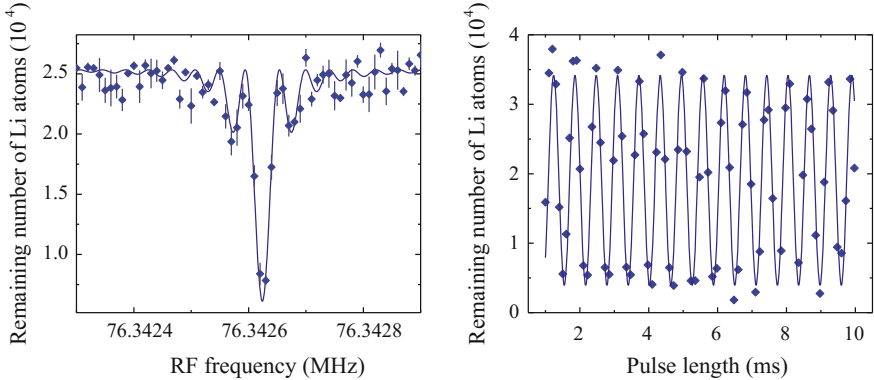


Fig. 2.7 Radio-frequency spectroscopy of $\text{Li}|1/2, +1/2\rangle$ to $\text{Li}|1/2, -1/2\rangle$ transition. *Left panel*, spectra of the transition with an rf-pulse length of 25 ms. The *solid line* shows the fit of Eq. (2.26) to the data. The fit yields a resonance frequency of $\omega_{ij}/(2\pi) = 76.34262$ MHz, which corresponds to a magnetic field of 888.535 G and a Rabi frequency $\Omega_0 = 2\pi \times 0.265$ Hz. *Error bars* correspond to one standard error. *Right panel*, Rabi oscillations of the same transition at a magnetic field of 841.430 G and a Rabi frequency of $2\pi \times 1.6$ kHz

$$P(\omega, t) = \left(\frac{\Omega_0}{\Omega_{\text{eff}}(\omega)} \right)^2 \sin^2 \left(\frac{\Omega_{\text{eff}}(\omega)}{2} t \right), \quad (2.26)$$

where Ω_0 denotes the Rabi frequency on the resonance, and $\Omega_{\text{eff}} = \sqrt{\Omega_0^2 + \delta^2}$ is the effective Rabi frequency with detuning $\delta = \omega_{ij} - \omega$. Here, ω_{ij} stands for the resonance frequency between the energy levels i and j and ω is the frequency of the driving field. A typical statistical error of the resonance frequency determination for a single spectrum is around a couple of mHz that corresponds to roughly 1 mG, if expressed in magnetic field uncertainty. This is at least an order of magnitude better than our total systematic error.

By recording the remaining number of Li atoms in the $\text{Li}|1/2, -1/2\rangle$ spin state as a function of the applied rf-pulse length, we observe Rabi oscillations, which are depicted in the right panel of Fig. 2.7. During the first 10 ms of the oscillations we do not observe any significant decay of decoherence, however longer measurements indicate time constants of around 200 ms, probably limited by dephasing through magnetic field inhomogeneities. At full power the setup can deliver Rabi frequencies of up to $2\pi \times 3.8$ kHz in the magnetic field region from 800 G to 900 G.

We use rf fields not only to perform high-precision spectroscopy, but also to gain greater control over the initial state preparation. By using π or $\pi/2$ pulses the population can be transferred between two states. Although theoretically 100 % transition efficiency can be achieved, in the experiment it can be limited by small drifts in the magnetic offset fields. Thus, instead of a coherent pulse, a rapid adiabatic passage can be realized that consists of sweeping the magnetic field over the resonance for a fixed rf frequency. The advantage of this approach is its inherent insensitivity of the exact values of the offset magnetic field at the beginning and end of the sweep. Therefore, this technique is used for the preparation of Li-Cs spin mixtures at 100 nK temperatures, which is described in Sect. 3.3.2. In principle, these methods could also be applied to obtain ultracold gas samples in scattering channels that initially are empty, and cannot be created by removal of impurity atoms, for example, channels involving $\text{Li}|3/2, -3/2\rangle$ or $\text{Cs}|3, +2\rangle$ spin states.

For experiments involving type (ii) transitions the final spin state is unpopulated, therefore the preparation sequence can be simplified, as additional spin cleaning procedure is not necessary. During the mw pulse a mixture consisting of Li atoms in three distinguishable spin states is created. As a drawback, fast three-body losses prevents one from observing coherent Rabi oscillations, since for typical experimental conditions the three-body recombination rate is much higher than the frequency of Rabi flopping. Additionally, the excitation of the higher lying $\text{Li } m_j = +1/2$ manifold leads to two-body inelastic collisions, since dipolar spin relaxation is now possible from the excited scattering channel into lower lying ones. A significant portion of the incoming scattering flux can exit through energetically lower lying scattering channels with high excess kinetic energy. Such atoms are typically lost from the trap, because their kinetic energy is larger than the depth of the confining potential.

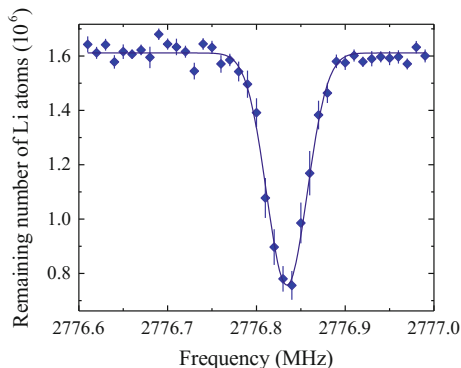


Fig. 2.8 Atom-loss spectrum of the microwave transition between $\text{Li}|1/2, -1/2\rangle$ and $\text{Li}|3/2, +3/2\rangle$ spin states at 935.151 G offset magnetic field. Each data point is an average of at least six independent measurements, and the *error bars* depict the standard error of the mean. The *solid line* shows the fit of a Gaussian profile to the data, yielding a variance of 23 kHz, which corresponds to 8 mG field uncertainty

Despite the atom losses, we employ type (ii) transitions to calibrate the magnetic field and determine the upper limit of magnetic field inhomogeneities in our setup. A typical spectrum for the transition between $\text{Li}|1/2, -1/2\rangle$ and $\text{Li}|3/2, +3/2\rangle$ spin states is shown in Fig. 2.8. The differential frequency shift of the transition amounts to $\approx 2.794 \text{ GHz/G}$ in this magnetic field range. The transition does not exhibit any coherent fringes, which is a combined result from a large atom loss rate and fast dephasing due to magnetic field inhomogeneities. A fit of a Gaussian profile to the spectrum yields FWHM of 54 kHz and resonance frequency of 2776.834 MHz. The latter corresponds to 935.151 G offset magnetic field. Since it is a complicated problem to separate between the contributions of individual line broadening mechanisms, we attribute the total linewidth to the rest-gradient of our magnetic field setup as a simplification. In this way we obtain an upper limit of 8 mG for the uncertainty on the offset magnetic fields due to inhomogeneities.

2.4 Radio-Frequency Association of Weakly-Bound LiCs Dimers

In the following section we investigate the interspecies scattering properties of ultra-cold Li-Cs mixtures in the two energetically lowest spin channels (see Eq.(2.11)) in the magnetic field range between 800 and 1000 G. The performed experiments on rf association and atom-loss spectroscopy to precisely measure the positions of the LiCs *s*-wave Feshbach resonances are described in Sect. 2.4.1. Depending on the width of the resonance we separate them into two groups and use complementary approaches to determine their properties. For the broad resonances close to 843 G

and 889 G we measure magnetic field dependent binding energies of weakly bound dimers through rf association. For the narrow resonances close to 816 G, 893 G, and 943 G we employ atom loss spectroscopy. Due to their small width the resonance position can still be detected with high accuracy. We use these measurements as an input for a coupled-channels (cc) calculation that allows us to construct accurate Li-Cs molecular potentials, from which scattering length a_{LiCs} , resonance pole positions and widths are determined. This procedure is explained in Sect. 2.4.3. The obtained parameters agree well with the previous observations [7, 13] and recent extensive theoretical studies [14].

The determined mapping between a_{LiCs} and the external magnetic field will be pivotal for further experiments exploring or involving ultracold scattering between Li and Cs atoms. Up to now, a precise s -wave FR parameterization existed only for pure Cs [35] and Li [27, 70] intraspecies scattering resonances, while Li-Cs interspecies collision properties were only approximately known from atom-loss measurements [7, 13, 14]. Rf spectroscopy experiments, that are described in the following section, bridge this gap. They allow to obtain precise FR parametrization also in a close vicinity of the pole of a Li-Cs scattering resonance. These results represent an order of magnitude improvement in accuracy over the previous determination. With this knowledge a complete description of the s -wave scattering properties in various three-body systems that can be constructed of Li and Cs atoms in the energetically lowest spin states is possible.

2.4.1 Spectroscopy of LiCs Feshbach dimers

We start our experiments with the sample preparation as described in Sect. 2.3.1. By slightly adjusting the dipole trap power in the last two evaporation ramps we reduce the temperature to about 400 nK. To associate the molecules we create a mixture in the non-resonant scattering channel at a variable magnetic field close to the FR in the resonant state (see Fig. 2.9). For the measurements close to the 843 G Li-Cs Feshbach resonance this corresponds to the initial scattering channel $|\beta\rangle$, from which the colliding atom pairs are associated into bound dimers that couple to the scattering channel $|\alpha\rangle$, as depicted in the left panel of Fig. 2.9. For the 889 G resonance we invert this sequence and start with the mixture in scattering channel $|\alpha\rangle$ and associate dimers that couple to channel $|\beta\rangle$, as schematically shown in the right panel of Fig. 2.9. In order to create the LiCs Feshbach molecules we drive the system with a rectangular rf pulse of length τ and frequency E_{rf}/h that is close to the resonance frequency E_0/h between the two energetically lowest Li spin states. By tuning the frequency of the rf photon, we record an atom-loss spectrum, which contains the number of remaining Li atoms in the non-resonant state as a function of the frequency of the applied rf field.

Each atom-loss spectrum contains two distinct loss features. At energies E_0 the free-free transition that corresponds to a flip of the Li nuclear spin is populating the other Li spin state. This creates a mixture of three distinguishable particles that consist

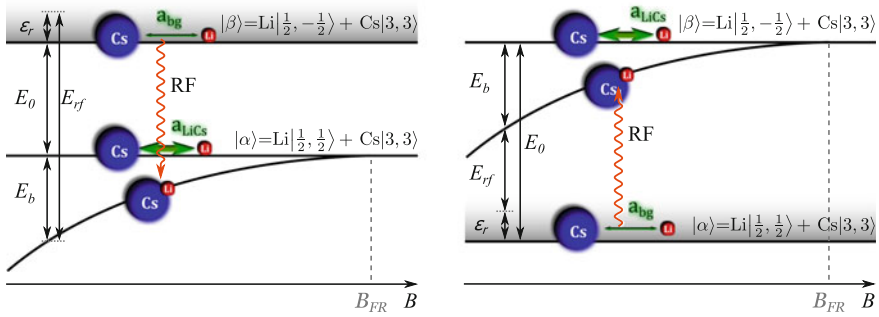


Fig. 2.9 Radio-frequency association of Li-Cs Feshbach molecules close to the 843 G (*left panel*) and 889 G (*right panel*) interspecies Feshbach resonance. The mixture is initially prepared in the non-resonant scattering channel $|\beta\rangle$ ($|\alpha\rangle$) at a magnetic field close to the broad 843 G (889 G) s -wave Feshbach resonance in the resonant scattering channel $|\alpha\rangle$ ($|\beta\rangle$), which couples to the weakly bound molecular state under study. Depending on the frequency of the rf driving field either the free-free transition with the energy E_0 or the free-bound transition with the energy $E_0 + E_b$ or $E_0 - E_b$ for the 843 G or 889 G FR, respectively, can be studied. The energy ε_r denotes the relative collision energy of the scattering Li-Cs atom pair, and typically is much smaller than the other energy scales. The vertical scaling does not correspond to the real energy scale and is modified for better presentation

of atoms in the following spin states: Cs $|3, +3\rangle$, Li $|1/2, 1/2\rangle$, and Li $|1/2, -1/2\rangle$. Since the scattering lengths at which these experiments are performed are large, rapid three-body loss can take place leading to a broad loss feature around the rf frequency E_0/h . The linewidth of this feature (see Fig. 2.11) is much larger than a typical linewidth of a magnetic field calibration line, for example, such as the one depicted in Fig. 2.7. Additionally, its position may be shifted due to residual Cs density, which may lead to a mean-field shift of the free-free transition energy that is proportional to a_{LiCs} . Therefore we do not use this transition for neither magnetic field calibration nor direct extraction of the molecular binding energies.

In a typical measurement procedure, we only record the free-bound spectrum, an example of which is shown for each of the broad Li-Cs FRs in Fig. 2.10. Detuned from the free-free transition (not shown), which corresponds to a flip of Li nuclear spin, we observe an additional loss feature that originates from the association of LiCs Feshbach dimers. During the rf-association pulse a mixture of LiCs Feshbach molecules and Li and Cs atoms in the initial scattering state is created, which leads to rapid three-body losses. The asymmetric lineshape originates from the relative collision energy distribution for the finite temperature of atoms, as explained in the next section. We also identify a similar loss signal at comparable values of detuning and amplitude in the remaining number of Cs atoms. To limit saturation effects the power and length τ of the association pulse is experimentally optimized such that at most 30 % of atoms are lost at the end of the rf pulse. The optimized pulse lengths range from $\tau = 0.5$ s close to the pole of the FR and $\tau = 7$ s away from it.

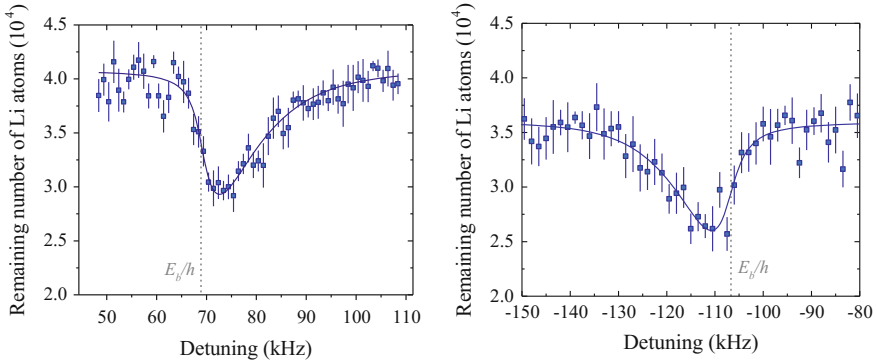


Fig. 2.10 Remaining number of Li atoms after an rf association (free-bound) pulse of LiCs molecules at a magnetic field of 842.04 G (*left panel*) and 887.599 G (*right panel*) for the broad s -wave resonance in $|\alpha\rangle$ and $|\beta\rangle$ scattering channel, respectively. For these measurements the relative Li-Cs temperature was 400 nK. Each data point is an average of three measurements and the *error bars* represent the standard error. The *solid line* shows the fit to the data. In the *left panel* the binding energy is determined from the fit of Eq. (2.27), while for the fit in the *right panel* appropriate transformation of $K_2^M(E_{rf})$ has been made (see text). The *vertical dashed line* corresponds to the fitted binding energy

For magnetic field values at which the dimer binding energy is smaller than $\lesssim 10$ kHz the molecule association lineshape starts to overlap with the one of the broadened free-free transition, therefore complicating extraction of binding energies. Such situation is depicted in Fig. 2.11. The loss feature of the free-free transition develops a shoulder at frequencies around 76.286 MHz, which indicates the formation of bound dimers. We extract the corresponding molecular signal by fitting the free-free spectrum by a Lorentzian profile in the regions far away from this feature and subtracting the result from the total loss spectrum. While this gives a strong indication that at these magnetic field values molecule formation is possible, precise determination of their binding energies is not feasible due to the strong influence of the free-free transition. The fitted binding energies significantly depend on the exact parameters of the fitted Lorentzian profile, therefore we exclude the spectra taken closer than 200 mG from the pole of the FR from the final analysis in Sect. 2.4.3.

2.4.2 Model of the association lineshape

We model the observed loss spectrum with the help of rate equations and a two-body association rate K_2^M [21, 71] that depends on the dimer binding energy. The long association pulse lengths and low molecule yield, which is below our detection limit, indicates that the dimer association rate is much smaller than their loss rate. Assuming a quasi-stationary state, in which each produced molecule immediately gets lost through atom-dimer collisions, the time dependent Li atom loss at a given

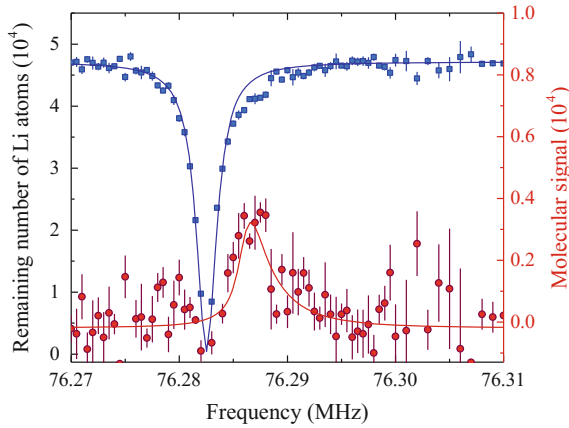


Fig. 2.11 LiCs dimer association spectrum at 842.761 G. The free-bound transition is overlapping with the strongly broadened free-free transition. The *blue rectangles* depict the remaining number of Li atoms in the $|\beta\rangle$ scattering state after a 500 ms long rf pulse, and the *blue solid line* is a fit of a Lorentzian profile to the data. The *red circles and line* show the molecular signal and a fit of Eq. (2.27) to the data, respectively. The fit yields $E_b/h = 3.3(2)$ kHz and $\gamma = 2.1(7)$ kHz. Each point is an average of at least three independent measurements and the *error bars* represent the standard error of mean

magnetic field is governed by K_2^M and thus can be described through the following equation

$$N_{\text{Li}} = N_{\text{Li}}^0 e^{-n_{\text{Cs}} K_2^M t}, \quad (2.27)$$

where N_{Li}^0 is the initial number of Li atoms in the non-resonant state, n_{Cs} denotes the density of the Cs gas cloud, t is the length of the applied rf pulse and K_2^M contains the functional form (see below) of the molecular association rate. Here we neglect single-body losses and assume constant n_{Cs} , which is justified by the fact that we are working in a low saturation limit of the rf transition. By solving the full system of rate equations we estimate that this approximation, using the simple Eq. (2.27), may introduce a minor error on the fitted atom loss amplitude, which does not exceed 10%. Since the number of produced LiCs molecules at any given point through the experimental cycle is insignificant, we do not include the loss terms associated with the molecule-molecule recombination.

The rf-association process is equivalent to photoassociation (PA), where an atom pair in an initial continuum state is associated into an excited vibrational level [72, 73]. One of the major differences is the lifetime of the involved final state, which is significantly lower in the PA scheme. Whereas in PA it is given by the spontaneous decay of the associated level, for rf-associated dimers it is typically limited by collisions. Since the natural linewidth of the rf-associated molecule is typically much smaller than the thermal energy scale, the association lineshape at ultracold temperatures contains information not only about the energy distribution of the initial scattering channel, but also its energy dependent Franck-Condon overlap with the

molecular state [71]. For a thermal ensemble that is prepared in the scattering state $|\beta\rangle$ the two-body association rate K_2^M can be expressed as

$$K_2^M(E_{rf}) = C \int_0^\infty h(\varepsilon_r) F(\varepsilon_r, E_b) L_\gamma(E_{rf}, E_0 + E_b + \varepsilon_r) d\varepsilon_r, \quad (2.28)$$

where $h(\varepsilon_r) \propto e^{-\varepsilon_r/k_b T}$ is the number density of colliding atom pairs with relative energy ε_r and temperature T , and

$$F(\varepsilon_r, E_b) \propto \left(1 - \sqrt{\frac{E_b}{E_b'}}\right)^2 \frac{\sqrt{\varepsilon_r E_b} E_b'}{(\varepsilon_r + E_b)^2 (\varepsilon_r + E_b')} \quad (2.29)$$

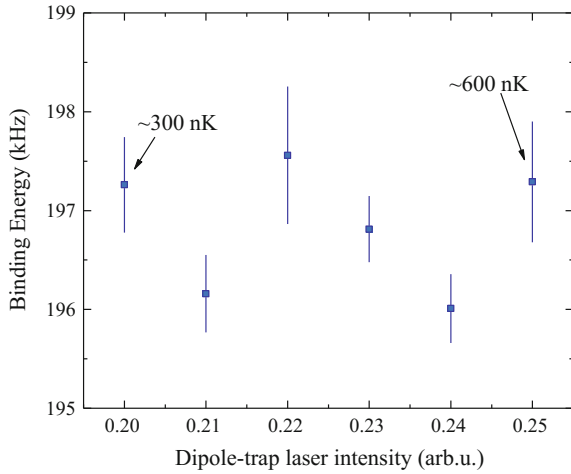
is the energy normalized Franck-Condon density between the scattering wave function of a free Li-Cs atom pair and a bound Feshbach dimer with binding energy E_b [21, 71]. E_b' is defined through the Li-Cs reduced mass μ and the non-resonant channel scattering length a' as $E_b' = \hbar^2/(2\mu a'^2)$. The convolution of the spectroscopic line shape with the Lorentzian profile $L_\gamma(E_{rf}, E_0 + E_b + \varepsilon_r)$ of width γ accounts for the strong collisional broadening, yielding an estimated lifetime of LiCs molecules in the mixture of around 30 μ s. The prefactor C contains all the numerical factors resulting from the integration of rate equations, and experimental parameters that affect the molecule production rate, but which are approximately constant for a given magnetic field, as well as species-dependent atom-dimer inelastic collision rates.³ It also accounts for uncertainties in the determination of the absolute gas densities, which, under realistic experimental conditions, can vary up to a factor of two due to systematic errors in measurements of the trap frequencies, temperature and the exact number of atoms.

The analysis of the atom-loss lineshape for a sample prepared in the scattering state $|\alpha\rangle$ is identical to the one presented above, with the sole exception that in this case the rf-photon energy needed for dimer association is smaller than the energy of the free-free transition (see Fig. 2.9, right panel). Consequently, the functional form of the association rate has to be adapted according to the energy conservation laws. The final expression for the association lineshape in state $|\alpha\rangle$ is obtained by the substitution $L_\gamma(E_{rf}, E_0 + E_b + \varepsilon_r) \rightarrow L_\gamma(E_{rf}, E_0 - E_b - \varepsilon_r)$, which is used for the fitting and analysis of dimer association lineshapes corresponding to the 889 G FR, as shown in the right panel of Fig. 2.10.

The binding energy of the Feshbach dimers at a given magnetic field is extracted by fitting Eq. (2.27) to the loss spectrum of Li atoms (see Fig. 2.10). We use E_b , N_{Li}^0 , γ , and C as free fitting parameters and set $a' = -28.5 a_0$ [7, 13, 14]. Small variations in a' that are of the order of a few of percent affect the fitted binding energies on a permille level. The temperature of each species is determined in an independent measurement with identical trapping parameters and is kept fixed during the fit.

³The prefactor C slightly depends on n_{Cs} and n_{Li} . For atom losses, which do not exceed $\approx 30\%$ of the initial number of atoms, it does not change by more than 5%.

Fig. 2.12 Binding energy as a function of the dipole-trap laser intensity at 841.5 G. The *error bars* depict the uncertainty of fitting Eq. (2.27) to the data. The corresponding temperature of the two limiting trapping settings is given in the graph next to the data points



To exclude systematic effects associated with the precise determination of relative temperature we verify that by increasing it by a factor of two the value of the fitted binding energy does not change by more than 1 kHz (see Fig. 2.12).

The extracted binding energy can be affected by several other systematic effects. One of them is the mean-field shift, which starts to dominate in the regime where the scattering length is comparable to the interparticle spacing, i.e. $na^3 \sim 1$. For our experimental densities of $n \approx 10^{11} \text{ cm}^{-3}$ such shifts would become relevant at magnetic field regions with binding energies on the order of $E_b \approx 1 \text{ kHz}$, which is sufficiently far away from the region where the experiments were performed. Additionally, by changing the background Cs atom density we verified that the observed molecular association line shifts stay within the statistical uncertainties of the fit, and therefore we do not include the mean-field shift in the analysis.

Another source of systematic resonance shifts is the confining optical dipole potential. The detuning of the dipole trap laser beam is large in comparison to the hyperfine splitting of the involved spin states, hence its created light shift is equal for both of them and can be neglected. However, the confining potential can contribute to the scattering state energy shift in two other ways. The first one is the confinement-induced shift of the relative ground state energy for two colliding free atoms. Its magnitude can be calculated for two interacting particles in a cigar shaped harmonic trap [74], and for our dipole trap geometry with aspect ratio $\eta \approx 9$ it yields 325 Hz. The second complication is the fact that, in contrast to two identical atoms [75], the problem of two different atoms in a harmonic trap with unlike trapping frequencies does not separate into center-of-mass and relative coordinates (see, for example, [76, 77]). The magnitude of the shift of the associated lowest energy state in a Li-Cs mixture can be estimated for our trapping geometry and mass-ratio, and is on the order of 50 Hz [76]. Since the order of magnitude of these corrections is much smaller than the measured binding energies we neglect these effects in the model that we use to fit the data, however, we include them in the total systematic error budget.

It has been recently demonstrated in the ${}^6\text{Li}$ - ${}^{40}\text{K}$ system that the scattering length, and thus the binding energy of the dimer can be manipulated by the differential light shift between the molecular and scattering state, leading to shifts in the FR positions [78]. In our measurements that were performed in the vicinity of the 843 G Li-Cs Feshbach resonance, no modification of the binding energies with respect to the intensity of the trapping light could be observed. The measured binding energy as a function of the potential depth can be seen in Fig. 2.12. The fluctuations of the data points give an independent estimation of the accuracy with which the binding energy can be extracted from the association spectra. We include these fluctuations as an additional statistical error in the total error budget, since the trapping parameters and temperature may slightly drift from day-to-day.

2.4.3 *Li-Cs scattering length and Feshbach resonances*

To obtain a complete set of Li-Cs s -wave FR properties we employ two different methods. Depending on the width ΔB of the particular FR either one or the other method is used to measure its position. Such experimental approach is feasible because FRs with different widths influence the scattering observables differently. Typically, the shift of the atom-loss maximum with respect to the true FR pole position can reach a couple permill of the resonance width ΔB (see, for example, the comparison of the atom-loss data with the binding energy measurement in the left panel of Fig. 2.13). For narrow FRs with a width of 5 G this corresponds to a shift of ~ 10 mG, which is on the order of our experimental uncertainty. For broad FR it can reach several hundreds of mG, which is significantly larger than our magnetic field uncertainty, therefore impeding a correct determination of the pole position. To overcome this, we use rf association to characterize broad FRs, and the simpler atom-loss measurements to probe narrow FRs.

By performing the measurements and the fitting procedure that were described in Sect. 2.4.2 for different external magnetic fields, we record the binding energy dependence on the external magnetic field, which is displayed in Fig. 2.13 for the two broadest FRs in the Li-Cs mixture.

We determine the positions of the narrow s -wave resonances in the magnetic range between 800 and 1000 G by atom-loss measurements, similar to the ones presented in Fig. 2.1. For these measurements we reach roughly an order of magnitude lower relative kinetic energies than in the previous works [7, 13]. Their experimental positions B^e are extracted from a Gaussian profile fit to each of the loss features in the magnetic field range where the line shape is approximately symmetric, and are summarized in Table 2.1. The improved magnetic field stability and lower temperatures allow us to determine them with a roughly five-fold better precision than in our previous measurement [7].

To obtain an accurate mapping between the scattering length and the magnetic field that is independent of the employed analytical fitting model [70], the data was

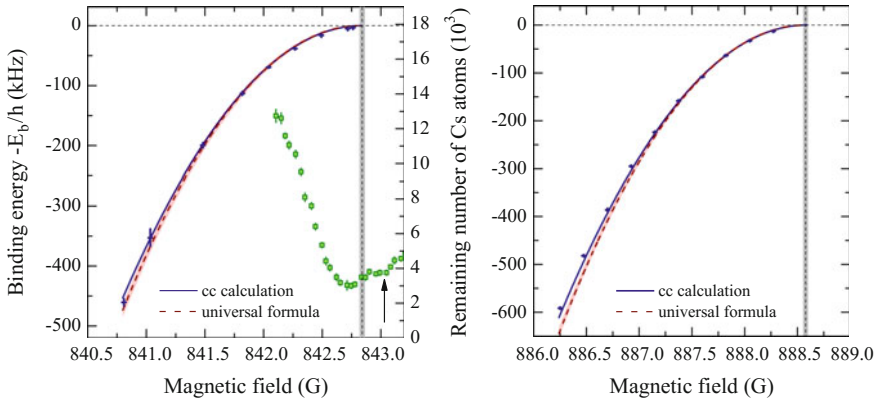


Fig. 2.13 Binding energies of LiCs Feshbach molecules near the 843 G (*left panel*) and 889 G (*right panel*) Feshbach resonance, and corresponding atom-loss spectroscopy. The *blue crosses* show the dimer binding energy as extracted from a fit of Eq. (2.27) to the rf association spectrum at the given magnetic field. The *error bars* represent one standard deviation of the total error, resulting from statistical and systematic uncertainties. The *blue* and *red solid lines* show the calculated molecular energies from the coupled-channels model and the universal binding energy from Eq. (2.24) with the resonance parameters given in Table 2.1. The *red shaded region* corresponds to the uncertainty of the resonance parameters. The *green squares* show the remaining number of Cs atoms, and the error corresponds to one standard error of the mean. The systematic magnetic field uncertainty for the atom loss measurements in this figure is 30 mG. The *vertical dashed line* displays the resonance pole position and the shaded region corresponds to the uncertainty. The arrow in the *left panel* shows the position of the second excited Li-Cs-Cs Efimov resonance with scattering length $a_-^{(2)}$

Table 2.1 Positions of the Li-Cs *s*-wave Feshbach resonances. Unless specifically noted, the experimentally obtained resonance positions B^e are extracted by fitting a Gaussian profile to the loss spectra for the relative collision temperature T , at which the measurements were made. The numbers in the brackets represent the total error that includes uncertainty of the magnetic field, and statistical and systematic errors of determining the position of the resonance. The results of the coupled-channels calculation B^t are given as deviations $\delta = B^e - B^t$ from the observations and show excellent agreement with the data. B_{FR} , ΔB , and a_{bg} give the fitted resonance pole position, width, and background scattering length, respectively, for the calculation with kinetic energy of 1 nK

Entrance channel	B^e (G)	δ (G)	T (nK)	B_{FR} (G)	ΔB (G)	a_{bg} (a_0)
Li 1/2, -1/2> \oplus	816.128(20)	-0.005	300	816.113	-0.37	-29.6
Cs 3, +3>	888.595(16) ^a	0.002	100	888.578	-57.45	-29.6
	943.020(50)	-0.033	400	943.033	-4.22	-29.6
Li 1/2, +1/2> \oplus	842.845(16) ^a	-0.000	100	842.829	-58.21	-29.4
Cs 3, +3>	892.655(30) ^b	0.005	100	892.629	-4.55	-29.4

^aExtrapolated from rf association. The temperature shown is only used for the calculation of the scattering resonance and selected sufficiently low to reduce its influence to less than 5 mG. The error reflects the uncertainty of the field calibration.

^bThis measurement was performed in the bichromatic dipole trap with species selective optical potentials, as described in Sect. 3.3.

analyzed with the full cc calculation⁴ for the Li(2s)+Cs(6s) asymptote as in the previous work [7, 14]. In short, the determination of the final resonance positions relies on the creation of accurate LiCs molecular potential curves for the electronic singlet $X^1\Sigma^+$ and triplet $a^3\Sigma^+$ ground states. The potentials are constructed as a power series of the internuclear separation R , as in previous calculations on other alkaline-metal systems (see, e.g., [55, 79, 80]), adding a short and long range part which gives the required degree of freedom for modeling the asymptotic binding energies. All coefficients are obtained by fitting. The correlation between the conventional long-range parameters C_6 , C_8 and C_{10} is still significant, thus they are only taken as effective parameters. The derived potential model simultaneously reproduces the binding energies of the Feshbach molecules, the refined s -wave FR positions B^e from atom loss experiments, and 6498 rovibrational transitions from laser-induced Fourier-transform spectroscopy [81]. We deduce the theoretical resonance positions B^t from the maxima of calculated two-body collision rates at the experimental kinetic energy.

For the binding energies below the 843 G resonance the two data points with the smallest binding energies are excluded from the fit. Their rf association spectra, due to experimental limitations, already overlap with the Li free-free transition spectra, which hinders a reliable extraction of the free-bound spectra for these respective magnetic field values, as discussed in Sect. 2.4.1 and shown in Fig. 2.11. Nevertheless, the calculated molecular binding energies are consistent with these data points, indicating that at these magnetic field values a weakly bound dimer state still exists.

The results of the modeling are listed in Table 2.1 as deviation $\delta = B^e - B^t$ from the measured positions for the experimentally employed relative collision temperature T and drawn as solid lines in Fig. 2.13. These results provide almost an order of magnitude improvement over the previous determination of the FR positions through the trap-loss measurements [7, 13] and the rf spectroscopy [82], and they are consistent with the recent theoretical analysis [14], if the differences in determining the resonance positions and experimental accuracy are taken into account.

Finally, we characterize the resonance profiles by calculating the scattering length dependence on the magnetic field at a kinetic energy of 1 nK and fitting this dependence with the conventional functional form

$$a(B) = a_{bg} \left(1 - \frac{\Delta B}{B - B_{FR}} - \dots \right) \quad (2.30)$$

with as many terms as there are resonances in the given channel. The resonance position B_{FR} , its width ΔB , and background scattering length a_{bg} are used as free fitting parameters, and they are given in Table 2.1. By including all observed resonances in a single fit of Eq. (2.30) one removes a possible slope of the effective background scattering length resulting from neighboring resonances. One could also fit the calculated profiles by a product of resonance functions, given by Eq. (2.21), for each

⁴We thank E. Tiemann from University of Hannover, Germany for performing these calculations for us.

resonance instead of the sum. This would result mainly in different values of ΔB , but as long as a consistent set of fitting function and corresponding parameters is used, the interpretation remains unchanged. The fitted values reproduce the calculated s -wave scattering length to better than 2 % in the entire magnetic field range between 500 and 1000 G, which we also use for the evaluation of the Efimov resonance positions in Chap. 3. There is a slight difference between the two theoretically obtained resonance pole positions B' and B_{FR} . We suspect that it originates from the different types of numerical calculations that were used to extract these parameters, however further investigation is necessary to find the exact reason behind this difference. Therefore we estimate the error for the resonance pole positions from the systematic error from the magnetic field uncertainty and the difference between the theoretical values, which yields ± 23 mG.

We use the obtained resonance parameters to plot the universal dimer binding energy from Eq. (2.24) in Fig. 2.13. The Li-Cs characteristic van der Waals energy scale [1] is $\hbar \times 157$ MHz, thus the influence of the short-range effects on the measured binding energies is minimal. This is reflected in the nearly ideal $1/a^2$ scaling of the measured binding energies in this magnetic field range. Since the Li-Cs background scattering length $a_{bg} \approx -29.5 a_0$ is small and negative, we expect only very minor influence of the virtual state in this regime. This contributes to the simple situation where the two LiCs binding energies are well described with the universal relation and can be treated independently from other neighboring resonances in the same scattering channels. This is in contrast to more complicated situations, like the one in Cs atoms where FRs overlap [32, 83].

The determined pole position of the 843 G FR clearly deviates from the previously observed atom loss maximum [82, 84], as shown in Fig. 2.13. It also deviates from the result $B_{FR} = 842.75(3)$ G obtained in [84], where exclusively atom loss measurements are used to infer the resonance pole position. This illustrates that the use of atom loss alone is questionable for a reliable determination of the FR pole position, especially if the resonance width is much larger than experimental uncertainties, as it is in the present case. The definition of the resonance pole position is based on pure two-body scattering. In real systems a number of different loss mechanisms may contribute to the total loss effect, the most prominent being the three-body collisions. The situation in the vicinity of the resonance's pole is complicated furthermore by the fact that not all of the inelastic three-body collisions result in an immediate loss of the atoms from the trap. Contribution from other recombination processes, for example, weakly-bound dimer formation and subsequent atom-dimer recombination, should be considered, which may lead to increased loss away from the pole of the FR. In this case the maximum of total atom losses can be shifted with respect to the maximum in the corresponding three-body loss rate [15, 16, 19]. The specific loss channels and the exact pathway of this decay in Li-Cs system still remain an open question, requiring a selective product state determination, which is not available at the present stage of our experiment. However, we expect that the shifts between the determined scattering pole positions and experimentally observed loss maxima can be explained or influenced by similar mechanisms as those discussed for other systems of ultracold gas mixtures [15–20].

References

1. C. Chin, R. Grimm, P. Julienne, E. Tiesinga, *Rev. Mod. Phys.* **82**, 1225 (2010)
2. T.Köhler, K.Góral, P.S. Julienne, *Rev. Mod. Phys.* **78**, 1311 (2006)
3. I. Bloch, J. Dalibard, W. Zwerger, *Rev. Mod. Phys.* **80**, 885 (2008)
4. P. Massignan, M. Zaccanti, G.M. Bruun, *Rep. Prog. Phys.* **77** (2014)
5. E. Braaten, H.-W. Hammer, *Phys. Rep.* **428**, 259 (2006)
6. Y. Wang, J.P. D’Incao, B.D. Esry, in *Advances in Atomic, Molecular, and Optical Physics*, vol. 62, Chapter 1, *Ultracold Few-Body Systems* (2013)
7. M. Repp, R. Pires, J. Ulmanis, R. Heck, E.D. Kuhnle, M. Weidemüller, E. Tiemann, *Phys. Rev. A* **87**, 010701 (2013)
8. R. Pires, *Efimov resonances in an ultracold mixture with extreme mass imbalance*, Ph.D. thesis, Heidelberg University (2014)
9. P.O. Fedichev, M.W. Reynolds, G.V. Shlyapnikov, *Phys. Rev. Lett.* **77**, 2921 (1996)
10. J.P. D’Incao, B.D. Esry, *Phys. Rev. Lett.* **94**, 213201 (2005)
11. J.P. D’Incao, B.D. Esry, *Phys. Rev. Lett.* **103**, 083202 (2009)
12. M. Repp, *Interspecies Feshbach resonances in an ultracold, optically trapped Bose-Fermi mixture of cesium and lithium*, Ph.D. thesis, Heidelberg University (2013)
13. S.-K. Tung, C. Parker, J. Johansen, C. Chin, Y. Wang, P.S. Julienne, *Phys. Rev. A* **87**, 010702 (2013)
14. R. Pires, M. Repp, J. Ulmanis, E.D. Kuhnle, M. Weidemüller, T.G. Tiecke, C.H. Greene, B.P. Ruzic, J.L. Bohn, E. Tiemann, *Phys. Rev. A* **90**, 012710 (2014)
15. K. Dieckmann, C.A. Stan, S. Gupta, Z. Hadzibabic, C.H. Schunck, W. Ketterle, *Phys. Rev. Lett.* **89**, 203201 (2002)
16. T. Bourdel, J. Cubizolles, L. Khaykovich, K.M.F. Magalhães, S.J.J.M.F. Kokkelmans, G.V. Shlyapnikov, C. Salomon, *Phys. Rev. Lett.* **91**, 020402 (2003)
17. C. Weber, G. Barontini, J. Catani, G. Thalhammer, M. Inguscio, F. Minardi, *Phys. Rev. A* **78**, 061601 (2008)
18. O. Machtey, D.A. Kessler, L. Khaykovich, *Phys. Rev. Lett.* **108**, 130403 (2012)
19. S. Zhang, T.-L. Ho, *New J. Phys.* **13**, 055003 (2011)
20. A.Y. Khramov, A.H. Hansen, A.O. Jamison, W.H. Dowd, S. Gupta, *Phys. Rev. A* **86**, 032705 (2012)
21. C. Klempt, T. Henninger, O. Topic, M. Scherer, L. Kattner, E. Tiemann, W. Ertmer, J.J. Arlt, *Phys. Rev. A* **78**, 061602 (2008)
22. C.A. Regal, C. Ticknor, J.L. Bohn, D.S. Jin, *Nature* **424**, 47 (2003)
23. M. Bartenstein, A. Altmeyer, S. Riedl, R. Geursen, S. Jochim, C. Chin, J.H. Denschlag, R. Grimm, A. Simoni, E. Tiesinga et al., *Phys. Rev. Lett.* **94**, 103201 (2005)
24. C. Ospelkaus, S. Ospelkaus, L. Humbert, P. Ernst, K. Sengstock, K. Bongs, *Phys. Rev. Lett.* **97**, 120402 (2006)
25. R.A.W. Maier, C. Marzok, C. Zimmermann, P.W. Courteille, *Phys. Rev. A* **81**, 064701 (2010)
26. C.-H. Wu, J.W. Park, P. Ahmadi, S. Will, M.W. Zwierlein, *Phys. Rev. Lett.* **109**, 085301 (2012)
27. G. Zürn, T. Lompe, A.N. Wenz, S. Jochim, P.S. Julienne, J.M. Hutson, *Phys. Rev. Lett.* **110**, 135301 (2013)
28. L. Huang, P. Wang, B.P. Ruzic, Z. Fu, Z. Meng, P. Peng, J.L. Bohn, J. Zhang, *New J. Phys.* **17**, 033013 (2015)
29. J. Fuchs, C. Ticknor, P. Dyke, G. Veeravalli, E. Kuhnle, W. Rowlands, P. Hannaford, C.J. Vale, *Phys. Rev. A* **77**, 053616 (2008)
30. S.T. Thompson, E. Hodby, C.E. Wieman, *Phys. Rev. Lett.* **95**, 190404 (2005)
31. S.B. Papp, C.E. Wieman, *Phys. Rev. Lett.* **97**, 180404 (2006)
32. A.D. Lange, K. Pilch, A. Prantner, F. Ferlaino, B. Engeser, H.-C. Nägerl, R. Grimm, C. Chin, *Phys. Rev. A* **79**, 013622 (2009)
33. G. Thalhammer, G. Barontini, J. Catani, F. Rabatti, C. Weber, A. Simoni, F. Minardi, M. Inguscio, *New J. Phys.* **11**, 055044 (2009)

34. N. Gross, Z. Shotan, S. Kokkelmans, L. Khaykovich, *Phys. Rev. Lett.* **105**, 103203 (2010)
35. M. Berninger, A. Zenesini, B. Huang, W. Harm, H.-C. Nägerl, F. Ferlaino, R. Grimm, P.S. Julienne, J.M. Hutson, *Phys. Rev. A* **87**, 032517 (2013)
36. P. Dyke, S.E. Pollack, R.G. Hulet, *Phys. Rev. A* **88**, 023625 (2013)
37. G.F. Gribakin, V.V. Flambaum, *Phys. Rev. A* **48**, 546 (1993)
38. K. Góral, T. Kähler, S.A. Gardiner, E. Tiesinga, P.S. Julienne, *J. Phys. B: At. Mol. Opt. Phys.* **37**, 3457 (2004)
39. J. Ulmanis, S. Häfner, R. Pires, E.D. Kuhnle, M. Weidemüller, E. Tiemann, *New J. Phys.* **17**, 055009 (2015)
40. C.J. Joachain, *Quantum Collision Theory* (Elsevier Science Ltd, 1984)
41. W. Ketterle, D.S. Durfee, D.M. Stamper-Kurn, in *Proceedings of the International School of Physics “Enrico Fermi”*, ed. by M. Inguscio, S. Stringari, C.E. Wieman (IOS Press, Amsterdam, 1999), “Making, probing and understanding Bose-Einstein condensates”, pp. 67–176
42. F. Schwabl, *Quantenmechanik* (Springer, 2007)
43. J. Dalibard, in *Proceedings of the International School of Physics “Enrico Fermi”*, ed. by M. Inguscio, S. Stringari, C.E. Wieman (IOS Press, Amsterdam, 1999), “Collisional dynamics of ultra-cold atomic gases”, pp. 321–349
44. L.D. Landau, E.M. Lifshitz, *Quantum Mechanics: Non-Relativistic Theory* (Pergamon Press, 1991)
45. J.J. Sakurai, J.J. Napolitano, *Modern Quantum Mechanics* (Addison-Wesley, 2010)
46. E.P. Wigner, *Phys. Rev.* **73**, 1002 (1948)
47. K. Aikawa, A. Frisch, M. Mark, S. Baier, A. Rietzler, R. Grimm, F. Ferlaino, *Phys. Rev. Lett.* **108**, 210401 (2012)
48. K. Aikawa, A. Frisch, M. Mark, S. Baier, R. Grimm, F. Ferlaino, *Phys. Rev. Lett.* **112**, 010404 (2014)
49. S. Stellmer, M.K. Tey, B. Huang, R. Grimm, F. Schreck, *Phys. Rev. Lett.* **103**, 200401 (2009)
50. J. Stuhler, A. Griesmaier, T. Koch, M. Fattori, T. Pfau, S. Giovanazzi, P. Pedri, L. Santos, *Phys. Rev. Lett.* **95**, 150406 (2005)
51. M. Lu, N.Q. Burdick, B.L. Lev, *Phys. Rev. Lett.* **108**, 215301 (2012)
52. H. Feshbach, *Ann. Phys.* **5**, 357 (1958)
53. U. Fano, *Phys. Rev.* **124**, 1866 (1961)
54. H.T.C. Stoof, J.M.V.A. Koelman, B.J. Verhaar, *Phys. Rev. B* **38**, 4688 (1988)
55. C. Strauss, T. Takekoshi, F. Lang, K. Winkler, R. Grimm, J. Hecker Denschlag, E. Tiemann, *Phys. Rev. A* **82**, 052514 (2010)
56. C. Ticknor, C.A. Regal, D.S. Jin, J.L. Bohn, *Phys. Rev. A* **69**, 042712 (2004)
57. A.J. Moerdijk, B.J. Verhaar, A. Axelsson, *Phys. Rev. A* **51**, 4852 (1995)
58. E. Timmermans, P. Tommasini, M. Hussein, A. Kerman, *Phys. Rep.* **315**, 199 (1999)
59. F.H. Mies, M. Raoult, *Phys. Rev. A* **62**, 012708 (2000)
60. A. Arias, *A reservoir optical dipole trap for creating a Bose-Einstein condensate of ^{133}Cs* , Master’s thesis, Heidelberg University (2014)
61. S. Häfner, *A tunable optical dipole trap for ^6Li and ^{133}Cs* , Master’s thesis, Heidelberg University (2013)
62. A. Schönhals, *Imaging of ultracold cesium atoms at high magnetic fields*, Master’s thesis, Heidelberg University, Germany (2013)
63. R. Heck, *All-optical formation of an ultracold gas of fermionic lithium close to quantum degeneracy*, Master’s thesis, Heidelberg University (2012)
64. V. Vuletić, C. Chin, A.J. Kerman, S. Chu, *Phys. Rev. Lett.* **81**, 5768 (1998)
65. A.J. Kerman, V. Vuletić, C. Chin, S. Chu, *Phys. Rev. Lett.* **84**, 439 (2000)
66. P. Treutlein, K.Y. Chung, S. Chu, *Phys. Rev. A* **63**, 051401 (2001)
67. P.W.H. Pinkse, A. Mosk, M. Weidemüller, M.W. Reynolds, T.W. Hijmans, J.T.M. Walraven, *Phys. Rev. Lett.* **78**, 990 (1997)
68. M. Hammes, D. Rychtarik, H.-C. Nägerl, R. Grimm, *Phys. Rev. A* **66**, 051401 (2002)
69. T. Weber, *Bose-Einstein condensation of optically trapped cesium*, Ph.D. thesis, University of Innsbruck (2003)

- 70. P.S. Julienne, J.M. Hutson, *Phys. Rev. A* **89**, 052715 (2014)
- 71. C. Chin, P.S. Julienne, *Phys. Rev. A* **71**, 012713 (2005)
- 72. R. Napolitano, J. Weiner, C.J. Williams, P.S. Julienne, *Phys. Rev. Lett.* **73**, 1352 (1994)
- 73. K.M. Jones, E. Tiesinga, P.D. Lett, P.S. Julienne, *Rev. Mod. Phys.* **78**, 483 (2006)
- 74. Z. Idziaszek, T. Calarco, *Phys. Rev. A* **74**, 022712 (2006)
- 75. T. Busch, B.-G. Englert, K. Rzażewski, M. Wilkens, *Found. Phys.* **28**, 549 (1998)
- 76. J.F. Bertelsen, K. Mølmer, *Phys. Rev. A* **76**, 043615 (2007)
- 77. F. Deuretzbacher, K. Plassmeier, D. Pfannkuche, F. Werner, C. Ospelkaus, S. Ospelkaus, K. Sen-
gstock, K. Bongs, *Phys. Rev. A* **77**, 032726 (2008)
- 78. M. Jag, M. Zaccanti, M. Cetina, R.S. Lous, F. Schreck, R. Grimm, D.S. Petrov, J. Levinsen,
Phys. Rev. Lett. **112**, 075302 (2014)
- 79. C. Marzok, B. Deh, C. Zimmermann, P.W. Courteille, E. Tiemann, Y.V. Vanne, A. Saenz, *Phys.*
Rev. A **79**, 012717 (2009)
- 80. T. Schuster, R. Scelle, A. Trautmann, S. Knoop, M.K. Oberthaler, M.M. Haverhals, M.R.
Goosen, S.J.J.M.F. Kokkelmans, E. Tiemann, *Phys. Rev. A* **85**, 042721 (2012)
- 81. P. Staunum, A. Pashov, H. Knöckel, E. Tiemann, *Phys. Rev. A* **75**, 042513 (2007)
- 82. R. Pires, J. Ulmanis, S. Häfner, M. Repp, A. Arias, E.D. Kuhnle, M. Weidemüller, *Phys. Rev.*
Lett. **112**, 250404 (2014)
- 83. K. Jachymski, P.S. Julienne, *Phys. Rev. A* **88**, 052701 (2013)
- 84. S.-K. Tung, K. Jiménez-García, J. Johansen, C.V. Parker, C. Chin, *Phys. Rev. Lett.* **113**, 240402
(2014)

Heteronuclear Efimov Scenario in Ultracold Quantum
Gases

Universality in Systems with Large Mass Imbalance

Ulmanis, J.

2017, XVIII, 125 p. 45 illus., 44 illus. in color., Hardcover

ISBN: 978-3-319-51861-9